Metal-based folded-thermopile for 2.5D micro-thermoelectric generators

Ibrahim Bel-Hadj, Zahia Bougrioua, Katir Ziouche

Preprint
*Sensors & Actuators: A. Physical **349**, 1 January 2023, 114090 (DOI: 10.1016/j.sna.2022.114090)*

Metal-based folded-thermopile for 2.5D micro-thermoelectric generators

Ibrahim Bel-Hadj, Zahia Bougrioua*, Katir Ziouche

Univ. Lille, CNRS, Centrale Lille, Polytechnique Hauts-de-France, UMR 8520, IEMN, Institut d'Electronique de Microélectronique et de Nanotechnologie, F-59652 Villeneuve d'Ascq, France.

** Corresponding author at IEMN, Institute for Electronics, Microelectronics and Nanotechnology, Avenue Poincaré, 59652 Villeneuve d'Ascq, France. Tel: +33 3 2019 7920.*
E-mail addresses; zahia.bougrioua@univ-lille.fr; ibrahim.bel-hadj@univ-lille.fr; katir.ziouche@univ-lille.fr

Abstract

We report on the simulation and fabrication of 2.5D micro-thermoelectric generators (µTEGs) with a thermopile topology periodically folded and distributed on a multi-membrane template, capable of harvesting lost heat directly into useful electrical energy. The originality of the folded thermopile is multiple: i/ it uses low-cost and eco-friendly alloy-based thermoelectrics (TEs) in the form of a series of $Ni_{90}Cr_{10}/Cu_{55}Ni_{45}$ thermocouples (TCs), ii/ in each TC both TE layers are stacked on top of each other allowing a better integration, iii/ the TCs are electrically associated in series and in parallel, reducing drastically the electrical resistance, iv/ the choice of membrane number permits to tune the module thermal resistance. All this results in an improvement of the conversion efficiency of the µTEG compared to our former all-Silicon planar modules. A finite element simulation allows defining the temperature distribution profiles in the module as a function of its dimensions. Several 2- and 3-membranes based µTEGs were fabricated using CMOS-compatible Silicon technology and characterized. In the best µTEG, the harvesting of 1 Watt of heat results in an output power density of 108.3 µW/cm^2. This corresponds to an efficiency factor of 6.82 10^{-3} µW.cm^{-2}.K^{-2} which is better than state-of-the-art metal-based modules.

Keywords: metallic thermoelectrics; planar thermopile; micro-thermoelectric generators; CMOS-compatible technology; thermal modeling; membranes.

1. Introduction

The recent progress of the internet of things (IoT) is leading to an increasing need for energy because of the large amount of connected sensors, which is estimated to reach more than 25 billion by 2030 [1]. Most of these sensors have traditionally been powered by batteries that require regular maintenance or replacement, raising their environmental impacts [2–4]. The energy harvesting technology development, for the powering of autonomous devices, is gradually becoming an absolute necessity. Micro-thermoelectric generators (µTEGs) are micro-devices that convert waste heat into useful electrical power directly without an intermediate process. Generally speaking, the active part of a typical thermoelectric (TE) device consists of an assembly of n-type and p-type semiconductor materials, connected electrically in series and thermally in parallel [5,6]. Their working principle is based on the Seebeck effect [7], which allows the direct conversion of temperature gradient into electrical voltage.

The conversion efficiency of µTEGs can be related to the so-called dimensionless figure of merit $zT = \alpha^2 T/\rho\lambda$, where T is the absolute temperature, α is the Seebeck coefficient, ρ is the electrical resistivity and λ is the thermal conductivity [5]. This figure of merit concept makes it possible to assess the ability of such TE devices to convert heat into electrical power. Thus, in thermoelectricity, great efforts have been paid on the optimization of the electronic and thermal transport properties of TE materials [8–13]. For a large variety of TE materials, zT values are rarely exceeding unity over a very wide temperature range [14]. This makes the efficiency of µTEGs lower than some other energy harvesting techniques such as photovoltaics [15]. Nevertheless, the abundance of heat in our environment makes them a good candidate for thermal energy harvesting. Furthermore, for many applications where the heat source is available, the conversion efficiency is not necessarily the most important criterion for evaluating the performance of the device: the output power of the µTEG is more relevant [16].

The emergence of new manufacturing technologies offers to µTEGs the possibility of having different shapes and sizes, built up with different materials and addressing new applications [17–19]. In general, µTEGs can be classified into two main categories depending on the thermocouple (TC) orientation relative to the surface: there are vertical and planar architectures. In the vertical structure, the TCs are arranged perpendicular to the flat surface of the substrate in contact with the heat source (or heat sink) [20–28]. This configuration has large heat-absorbing surfaces that allows providing more electrical output power. However, the large surface area of these vertical TE modules gives them a very low thermal resistance compared to the one of planar structures. Also, these

configurations are complex to manufacture and require significant technological resources which greatly limit their development [29]. On the other hand, the planar configuration of TE miniature modules generally uses thin-film thermoelectrics deposited by microfabrication processes, allowing to exploit temperature gradients that are generated within the very thin suspended structures [30–39]. *The planar configuration is beneficial to achieve high thermal resistance that can be adjusted with the TC length.* This allows adapting the µTEG to the thermal environment, in order to maximize the collected heat. Moreover, the use of TE thin films results in a small amount uptake of material and thus reduces the costs, which is important in the case of expensive and/or rare materials. Yet, their main disadvantage is related to the thermal and electrical contact resistances at the interfaces, which require a particular control in the fabrication of this type of structures [40].

In this article, we report on the design, the modeling, the fabrication and the characterization of a new family of planar µTEGs for thermal energy harvesting. The implemented technology is a CMOS-compatible microfabrication process, using low cost, abundant and environmentally friendly materials. It is based on an original topology of the thermopile with a high integration density and this thanks to a particular arrangement of the TE materials: each individual TC has a stacked configuration of its two thermoelements. To our knowledge this kind of stack have been used only by S. M. Yang *et al.*[39,41]. In order to reduce the electrical resistance of the µTEGs, we fabricate a thermopile that combines *series and parallel electrical integration* of the TCs. Also this resistance is further minimized by the use of p and n type metallic alloys, respectively $Ni_{90}Cr_{10}$ and $Cu_{55}Ni_{45}$, as both thermoelements, instead of the polySilicium/metal couple that we employed in our anterior work [33,42,43].

2. Thermopile and module topologies

2.1 Folded thermopile

The thermopile structure developed in this work is schematized in Fig. 1. It is made on a Silicon substrate passivated with a SiO_2/Si_xN_y bilayer. The surface of the module is chosen to be 1/3 cm² ($A_{\mu TEG}$= 6×5.7 mm²). The topology is based on a stack of three levels. The first level consists of metallic strips of $Ni_{90}Cr_{10}$, so-called Chromel, representing the first TE material (Fig. 1(a)). The second level is a thin SiO_2 layer, which will be embedded between both TE layers to insulate them in the verticality, except at two corners of each TC (Fig. 1(b)) where the electrical connection takes place at the TE junctions. The third level contains the second TE material, which is Constantan $Cu_{55}Ni_{45}$, periodically deposited on the $Ni_{90}Cr_{10}$ strips, as illustrated by the final shape of the thermopile presented in Fig. 1(d). In between both TEs junctions, a thin Au layer is used to ensure a good electrical

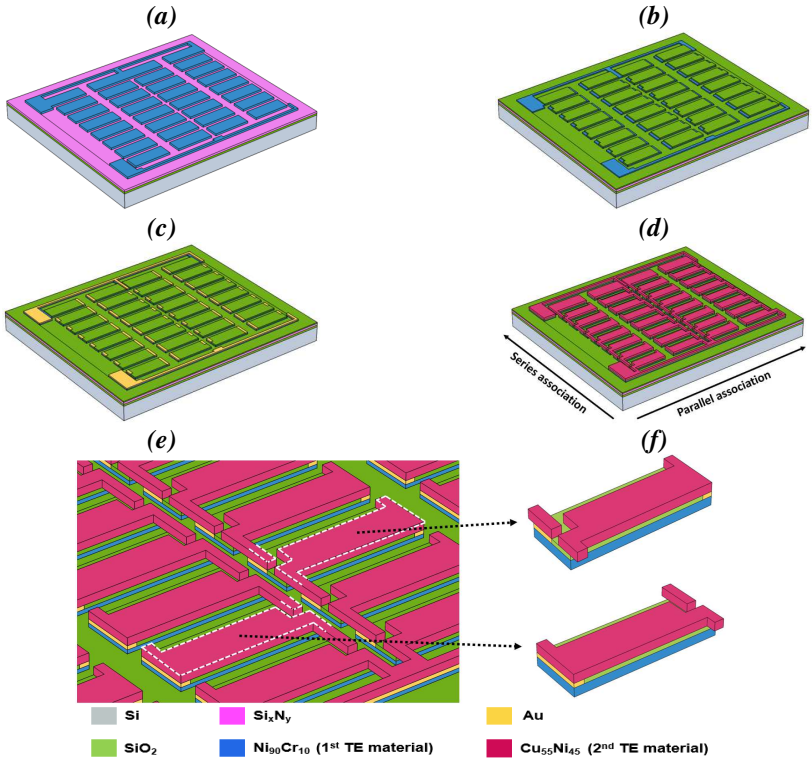

***Fig. 1** : Description of the new thermopile. (a) Schematic view of $Ni_{90}Cr_{10}$ strips presenting the first TE material; (b) SiO_2 isolation between the thermoelements; (c) Metallic Au contacts at the junctions between thermoelements and contact pads; (d) Schematic view of $Cu_{55}Ni_{45}$ strips (second TE material); This represents the case of a thermopile with 32 TCs which series/parallel association is given by the arrows; (e) Zoom of previous figure; (f) Two views to illustrate the original topology of a single TC.*

contact (Fig. 1(c) and (f)). The vertical assembly of the two thermoelements of each TC gives *the "periodical folded" character* of the thermopile. Also, each TC has a smaller footprint area, equivalent to the area of a single thermoelement. This increases the integration density of TCs compared to our former classical planar µTEG configuration [33,42,43]. Furthermore, the selected TE materials, $Ni_{90}Cr_{10}$ and $Cu_{55}Ni_{45}$, present a good compromise between their elaboration costs, their Seebeck efficiency and their advantage of being non-toxic and abundant.

2.2 Benefit of series/parallel association in the thermopile

We also designed a specific pattern for the thermopile where several TCs electrically associated in series, form multiple strips (or branches) connected in parallel (see Fig. 1(d) and a zoom in Fig. 1(e)). This series/parallel association of the TCs is implemented in order to reduce the total electrical resistance of the thermopile compared to the one of a purely series association, as explained in Fig. 2.

Indeed, if each TC is modelled by its equivalent electrical schema (with R_{TC} its electrical resistance), then a thermopile with a purely series association of N_{TC} thermocouples (on the left of Fig. 2), and a thermopile with a series/parallel association of the same number of TCs (on the right of Fig. 2, new thermopile topology) will have i/ a different internal electrical resistance R_{int} and ii/ a different output voltage delivered by the whole thermopile V_{out}. This latter is a function of the voltage at each TC and of the number of TCs in one strip, N_S: $V_{out} = N_S V_S$ and $V_S = \alpha_{TC}\Delta T_{hc}$, where ΔT_{hc} is the temperature gradient at each TC. However, the expression of the maximum output power, P_{max}, corresponding to the electrical power thermogenerated to a matched load resistance: $P_{max} = V_{out}^2/4R_{int}$, will be identical. Both quantities R_{int} and P_{max} can be expressed as a function of the individual TC parameters as given by the relations in Fig. 2 and its caption. So, in the case of the novel series/parallel TCs association, R_{int} can be tuned by fixing the number of branches connected in parallel, N_p (it is N_p^2 lower than in a series thermopile) while kipping the same value for P_{max}.

Moreover, the parallel association ensures electrical continuity (in at least one of the strips) in the case of an accidental cut in the connection between the thermocouples within one or more branches, which is a major problem in the purely series thermopile configuration.

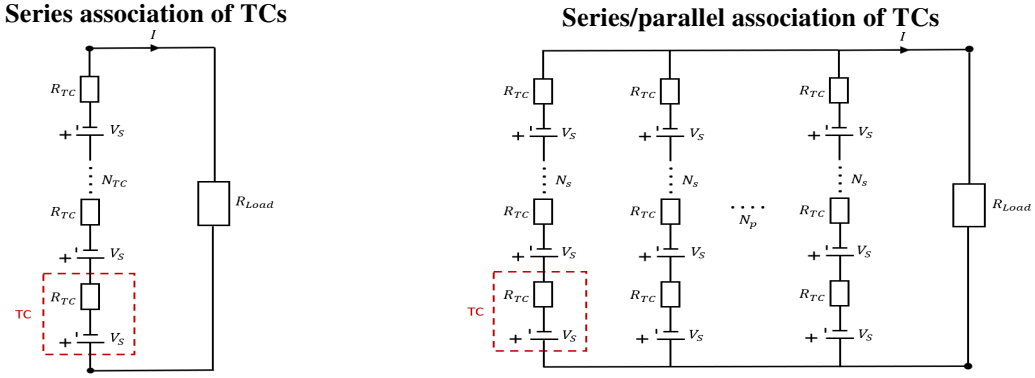

***Fig. 2** : Equivalent electrical schematic of a thermopile, comparing the internal electrical resistance (R_{int}) and the maximum output power (P_{max}) between the case of a purely series association and the case of a combined series/parallel association of TCs; N_{TC}: total number of TCs; N_s: number of TCs connected in series; N_p: number of strips connected in parallel; R_{TC}: electrical resistance of a single TC. V_S: Seebeck voltage of a single TC.*

2.3 The 2.5D module

The Si template that holds the folded thermopile is periodically etched to delimitate membranes that will enable the build-up of a temperature gradient at each TC from any incident multidirectional heat from the environment. Owing to our series/parallel thermopile design, this implies that the number of membranes (noted M) will be equal to $N_p/2$. The incident heat will be periodically concentrated on the top of the hot junctions of the thermopile via the pillars of a "Heat Concentrator" tailored within another Si wafer, as for our first family of µTEG modules which included polysilicon/gold TCs (see for instance fig.2 in [42], the case of a 3-membranes based module).

The µTEG final topology, integrating the described thermopile, is shown with various views in Fig. 3 in the case of 2 membranes (N_p=4). The overall module has a so-called 2.5D architecture. Indeed the bottom part of the

module consists of a set of multilayered membranes periodically distributed on an etched Si substrate, which will be a natural "evacuator" of the heat. As shown in Fig. 3(a), these membranes contain a SiO_2/Si_xN_y bilayer (with compensated stress using thicknesses of 800 nm and 600 nm respectively [44]), the planar thermopile and a thick Polyimide (PI) layer (~ 12 µm), that is used as a passivation and electrical isolation layer between the thermopile and the heat concentrator. The PI layer also contributes to the membranes robustness. This whole µTEG bottom part is covered by an upper cap as shown in Fig. 3(b): the Si-based heat concentrator (surface = 5.7×5.2 mm²) is build up with as much pillars as membranes (ie. $N_p/2$), and it will allow to canalize the harvested heat flow through half of the thermopile junctions (contacts are located at the hot junctions of the thermopile as shown in Fig. 3(c)). *One can remark that the choice of TC length will fix the number of membranes*. The air cavities located on both sides of membranes (230µm and 380 µm thick resp. on top and on the bottom), allow the thermal insulation of the hot and cold junctions of the thermopile (with the heat sink and the concentrator, respectively).

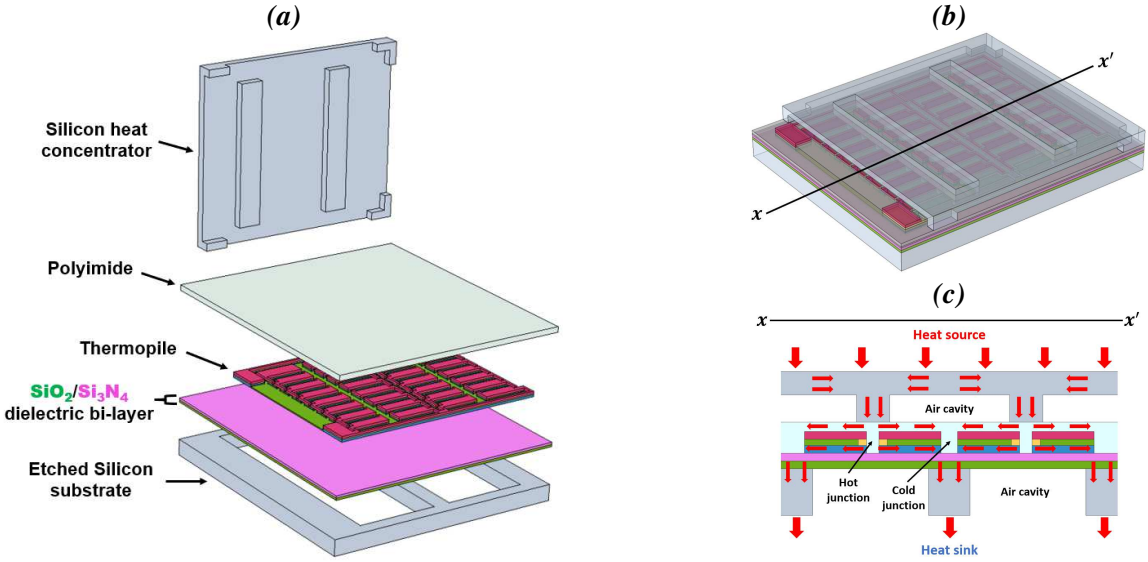

***Fig. 3** : (a) 3D exploded view (not to scale) of a 2.5D µTEG, in the case of 2-membranes and 32 TCs; (b) Skinned view of the structure ; (c) Cross-section view at xx' axis depicted in (b). For a 3-, 4- or M-membranes module the substrate will display 3, 4 or M cavities, the thermopiles 6, 8 or 2M strips and the heat-concentrator 3, 4 or M pillars.*

Mechanical supports, called bosses, placed at the 4 corners of the concentrator (visible in Fig. 3(a) and (b)), are used to ensure its rigid support onto the Si substrate and avoid membranes breaking. However, these 4 direct contacts on the module template lead to predictable lateral heat losses from the total heat flux collected onto the concentrator. These lateral losses do not contribute to the hot junction heating.

3. Finite element modeling of the µTEG

3.1 Basic considerations of the model

The µTEG structure we just described before, that integrates the folded thermopile architecture, was modelled using COMSOL Multiphysics® software based on the finite element methods (FEM). Indeed, this permits *predicting the temperature distribution and thermal resistance of the new planar µTEG* for a heat flux injected into the heat concentrator. Generally speaking, using *Heat Transfer Module* in COMSOL Multiphysics®, the temperature distribution is calculated by solving the heat equations in both solid and fluid domains, which can be expressed respectively as follow [45]:

$$\rho C_p \frac{\partial T}{\partial t} - \vec{\nabla} \cdot (\lambda \vec{\nabla} T) = Q \qquad (1)$$

$$\rho C_p \frac{\partial T}{\partial t} + \rho C_p \vec{u} \cdot \vec{\nabla} T - \vec{\nabla} \cdot (\lambda \vec{\nabla} T) = Q \qquad (2)$$

where ρ, C_p, T, λ, Q, and $\vec{u}$ represent the density, specific heat capacity at constant pressure, temperature, thermal conductivity, heat sources, and fluid velocity, respectively.

To simplify the model and reduce the computational time, some assumptions have been considered in this study, while ensuring there is no significant difference from real conditions. First, the materials used in the model are considered isotropic and homogeneous; their thermal conductivities are assumed independent of temperature. The temperature of the heat sink is assumed to be constant and equal to the ambient temperature, ie. 298K (perfect heat sink). We assume that the steady state is reached, ie. the temperature does not change with time ($\partial T/\partial t = 0$). Therefore, the first term of the equations (1) and (2) disappears. Moreover, considering the low height of the top

and the bottom air cavities around the membranes (as seen before only a few hundred microns thick), we will assume that the velocity of the air enclosed in these cavities is zero ($\vec{u} = \vec{0}$). Under these conditions, the equations (1) and (2) are reduced to a single simplified heat transfer equation, $-\vec{\nabla} \cdot (\lambda \vec{\nabla} T) = Q$, to be solved in all domains of the geometry.

The complex design of the thermopile, that can integrate a large number of TCs (up to several hundred TCs), does not allow a crude modeling of the geometry, which is by far exceeding the computational capabilities of our machines. Moreover, owing to the very low thickness of the layers (case of $Ni_{90}Cr_{10}/SiO_2/Cu_{55}Ni_{45}$ and SiO_2/Si_xN_y, each sublayer being less than 1µm), inherent difficulties occur in the generation of the modeling mesh and it limits the calculation convergence. For all these reasons, we consider the sub-layers, associated to the thermopile and the bilayer SiO_2/Si_xN_y, as *a continuous and thermally uniform "equivalent layer"*. This essential concept of the equivalent layer is detailed in the following paragraph.

3.2 Equivalent layer model

Taking into account i/ the symmetry of heat propagation directions across the whole module and its membranes (Fig. 3(c)), and ii/ the periodicity of the thermopile structure observed in the two transverse directions (x and y), we define the equivalent layer as shown in Fig. 4. Each membrane, whose constitution is complex, is assimilated to two continuous layers: the first one corresponds to the Polyimide layer and the second one is defined as the "thermal equivalent" layer to the other sub-layers constituting the membrane, ie. the $Ni_{90}Cr_{10}/SiO_2/Cu_{55}Ni_{45}$ stripes and the SiO_2/Si_xN_y bilayer. This unique second material will be defined by an equivalent thermal conductivity λ_{eq} and its thickness e_t (this latter being the sum of the thicknesses of all the sub-layers).

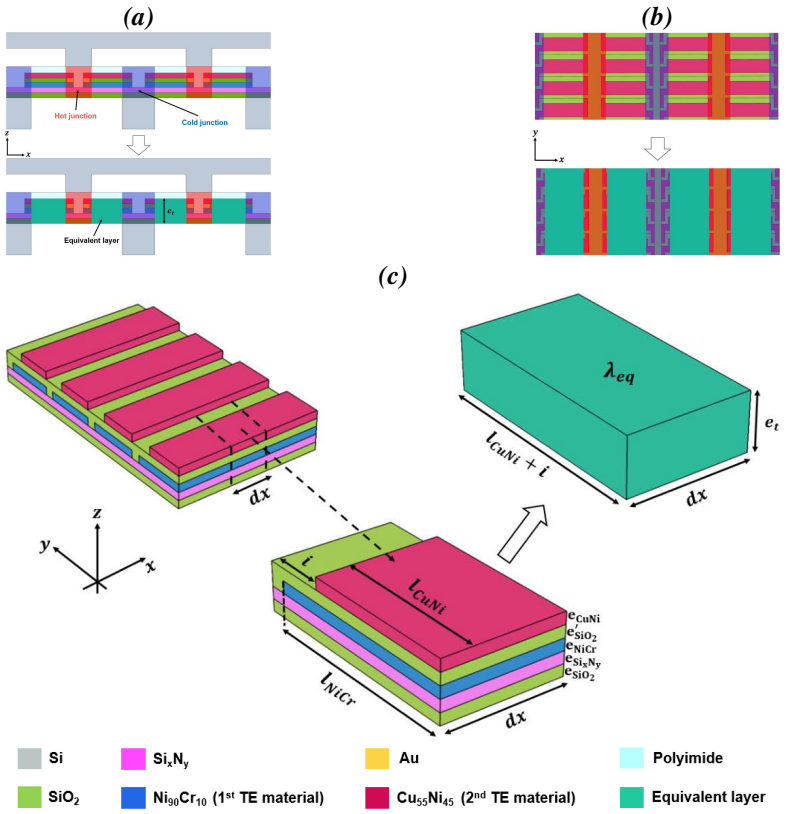

***Fig. 4** : Equivalent layer. (a) Cross-section shows the materials constituting the equivalent layer; (b) Top view of a part of the thermopile illustrating the periodicity of the thermopile in the two transverse directions x and y; (c) Construction of the equivalent layer from an elementary cell of the thermopile seen between two consecutive hot and cold junctions.*

In order to calculate the temperature distribution along the membrane using COMSOL Multiphysics®, we must first calculate λ_{eq}. Considering an elementary cell made up of the sub-layers constituting the equivalent layer, of length dx and width $l_{CuNi} + i$, seen between two consecutive hot and cold junctions (Fig. 4(c)), the total thermal conductance K_{eq} of the elementary equivalent layer is given by the sum of the thermal conductance of each material constituting the multilayer as:

$$K_{eq} = K_{SiO_2} + K_{Si_xN_y} + K_{NiCr} + K_{CuNi} \qquad (3)$$

where K_{SiO_2}, $K_{Si_xN_y}$, K_{NiCr} et K_{CuNi} are the elementary thermal conductance of the SiO_2, Si_xN_y, $Ni_{90}Cr_{10}$ and $Cu_{55}Ni_{45}$ layers given respectively by:

$$K_{SiO_2} = \frac{\lambda_{SiO_2}}{dx}(e_{SiO_2} + e'_{SiO_2})(l_{CuNi} + i) \quad (4)$$

$$K_{Si_xN_y} = \frac{\lambda_{Si_xN_y}\, e_{Si_xN_y}\, (l_{CuNi} + i)}{dx} \quad (5)$$

$$K_{NiCr} = \frac{\lambda_{NiCr}\, e_{NiCr}\, l_{NiCr}}{dx} \quad (6)$$

$$K_{CuNi} = \frac{\lambda_{CuNi}\, e_{CuNi}\, l_{CuNi}}{dx} \quad (7)$$

where λ, e, l et i are the thermal conductivity, the thickness, the width and the spacing between $Cu_{55}Ni_{45}$ strips (Fig. 4c) respectively. On the other hand, the equivalent thermal conductance K_{eq} is given by (Fig. 4(c)):

$$K_{eq} = \frac{\lambda_{eq}\, e_t\, (l_{CuNi} + i)}{dx} \quad (8)$$

with $$e_t = e_{SiO_2} + e_{Si_xN_y} + e_{NiCr} + e'_{SiO_2} + e_{CuNi} \quad (9)$$

By identification between the two expressions of K_{eq} given by (3) and (8) and taking into account the expressions given by (4), (5), (6), (7), and (9), the equivalent thermal conductivity can be written as:

$$\lambda_{eq} = \frac{\lambda_{SiO_2}(e_{SiO_2} + e'_{SiO_2}) + \lambda_{Si_xN_y}e_{Si_xN_y} + \lambda_{NiCr}e_{NiCr}\frac{l_{NiCr}}{l_{CuNi}+i} + \lambda_{CuNi}e_{CuNi}\frac{l_{CuNi}}{l_{CuNi}+i}}{e_{SiO_2} + e_{Si_xN_y} + e_{NiCr} + e'_{SiO_2} + e_{CuNi}} \quad (10)$$

The Table 1 summarizes an example of typical values of the geometrical dimensions and thermal conductivities of the materials constituting the equivalent layer. Using such values, *the calculated equivalent thermal conductivity is* $\lambda_{eq} = 8.58\ W.m^{-1}.K^{-1}$.

Parameter	Value	Unite
e_{SiO_2}	800	nm
e'_{SiO_2}	150	nm
$e_{Si_xN_y}$	600	nm
e_{NiCr}	150	nm
e_{CuNi}	450	nm
l_{NiCr}	200	µm
l_{CuNi}	150	µm
i	55	µm
λ_{SiO_2}	1.25 [46]	$W.m^{-1}.K^{-1}$
$\lambda_{Si_xN_y}$	12 [47]	$W.m^{-1}.K^{-1}$
λ_{NiCr}	17 [48]	$W.m^{-1}.K^{-1}$
λ_{CuNi}	23 [48]	$W.m^{-1}.K^{-1}$

Table 1 : Typical geometrical dimensions and thermal conductivities of the materials constituting the equivalent layer.

3.3 Modeling analysis

In practical conditions, the µTEG performance will be evaluated experimentally using a calibrated injected heat flux. To be able to do so, a gold-based heater, meander shaped, is realized on the top surface of the concentrator (will be presented in section 4.1). In order to simplify the calculation, this heater is modeled as a heat source uniformly distributed over the concentrator surface (Neumann boundary condition). As the µTEG is also exposed to the ambient, a part of the heat dissipated in the heater will be exchanged by convection and radiation with the outside environment. Boundary conditions were applied between the top surface of the concentrator and the ambient environment to take into account of all these exchanges. The heat transfer coefficient is set to be 25 $W.m^{-2}.K^{-1}$ (which corresponds to natural convection), the emissivity is set at 1 (ie. very conservative case; in reality it is likely around 0,5 to account for both large emissive nature of SiO_2 coated Si, and quasi-zero emissivity of the area covered by the Au heater), and the ambient temperature is 298 K. On the other hand, the bottom surface of the substrate, in contact with the heat sink, is also set to the ambient temperature (Dirichlet boundary condition). Moreover, the µTEG structure has a symmetry plane introduced by the equivalent layer model, which allows us to *consider just one half of the module* by adding an extra symmetry boundary condition as shown in Fig. 5. This consideration reduces the calculation time and the computer memory requirements.

Finally, the two thermal contacts i/ between the concentrator pillars (and bosses) and the part of the thermopile held on membranes (see Fig. 4.a) and ii/ between the thermopile template (ie. etched Si substrate) with the heat sink, are not perfect and cannot be neglected. Henceforth, in the modelling, a thermal contact boundary condition

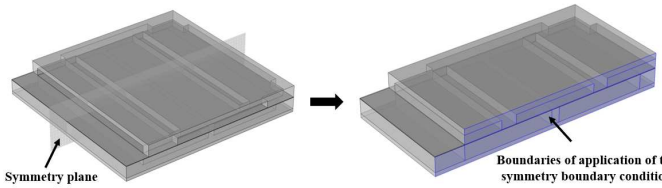

***Fig. 5** : Symmetry plane and half of the µTEG structure with the symmetry boundary condition.*

is applied to both those contact boundaries. The experimental results from the characterizations of µTEGs allow estimating the range of the thermal contact resistance, and this by confronting the experimental results with those of simulation. For instance, this one is estimated to be around 3.7 K.cm^2/W for a µTEG with 3 membranes.

In Fig. 6 is given the COMSOL® calculated temperature distribution on a half module, in the case of µTEGs with 2 and 3 membranes when a heat input power of 1 W is applied on the concentrator surface (which corresponds to a flux density of 3.3 W/cm²). So one can see how this heat flux injected is canalized through the membranes by the concentrator pillars, and creates periodic temperature gradients between the concentrator and substrate pillars. A part of the heat flux is canalized to the heat sink through the bosses (heat losses).

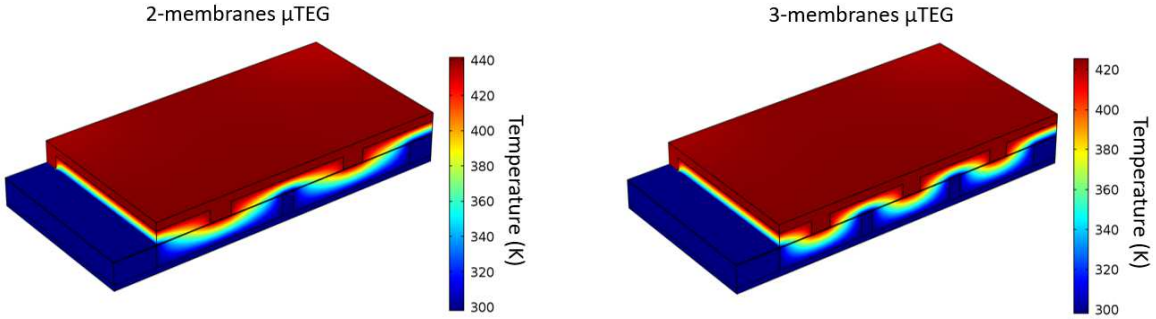

***Fig. 6** : Temperature distribution calculated for 2 and 3-membranes µTEGs. 1 W input power is injected into the concentrator and the temperature of the bottom side of the substrate is fixed at 298 K.*

The simulated results corresponding to the applied boundary conditions, allow *to anticipate by calculation that the temperature difference generated between the hot and cold junctions*, noted ΔT_{hc} (see Fig. 7(b)), are ΔT_{hc} = 137 K and 120 K (ie. decrease with the membrane number), and that those between the surface of the concentrator and the heat sink (noted ΔT_{HC}) are obviously higher: 142 K and 126 K, respectively for the 2- and 3-membranes µTEGs. The gap between ΔT_{hc} and ΔT_{HC} values is mainly due to the thermal contact resistances between the concentrator pillars and the membranes, and the heat losses across the bosses. To be precise, the percentages of the fluxes exchanged by convection, radiation and through the bosses are respectively evaluated to be of 11 %, 5 % and 37 % for the 2-membranes µTEG and of 9 %, 4 % and 33% for the 3-membranes µTEG. If the two first fluxes can be considered small (especially radiation and this would be even lower if we considered an emissivity ε<1), this is clearly not the case of the heat flow lost through the bosses.

Fig. 7(a) illustrates the isothermal distribution of the temperature field obtained on the half structure of a 2-membranes µTEG. The isothermal line distribution across the membranes, determined by simulation, shows that the planar temperature profile (x and y directions) depends only on the x direction. In contrast, at the proximity of the concentrator pillars and the edge of the membranes, there is naturally a slight deformation of the isothermal temperature profile along the y axis. Fig. 7(b) displays the transverse temperature profile (x and z directions), seen along two adjacent cold/hot junctions. We notice an homogeneous mapping of the temperature at the level of the concentrator and of the substrate (heat sink) due to the high thermal conductivity of the major material used, ie. Silicon (~ 140 W.m^{-1}.K^{-1}). *This mapping shows the important role of the air cavities located on both sides of each membrane*, which allow an efficient insulation of the hot and cold junctions of the thermopile.

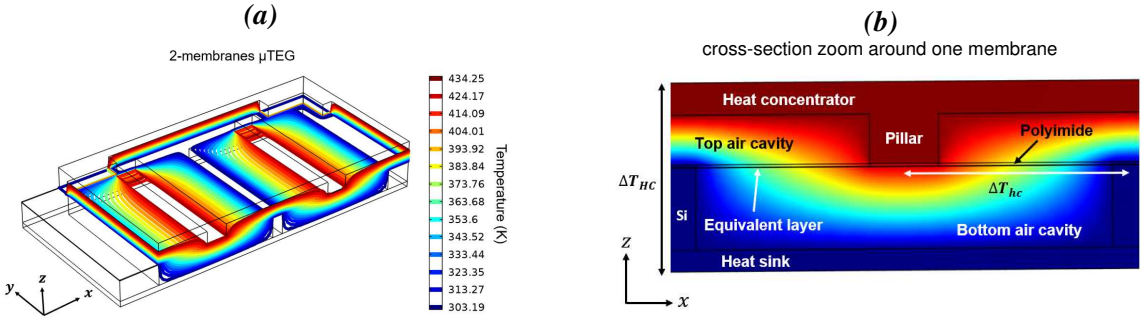

***Fig. 7** : (a) Isothermal field distribution obtained on the half structure of the 2-membranes µTEG; (b) Symmetrical 2D cross-section seen between consecutive hot-cold junctions of one TC.*

.So, this numerical calculation of the temperature distribution across the 2.5D µTEG, permits to predict the relation between the two gradients ΔT_{hc} and ΔT_{HC}, this latter being experimentally difficult to measure while only ΔT_{hc} is accessible, as by definition it is related to the experimental output voltage, $V_{out} = N_S \alpha_{TC} \Delta T_{hc}$.
The knowledge of ΔT_{hc} allows to deduce analytically the predicted maximum output power, P_{max}, generated by the µTEG. This is the *key quantity to study and to optimize* and $P_{max} = N_s^2 \alpha_{TC}^2 \Delta T_{hc}^2 / 4R_{int}$ as seen in section 2.
For the two µTEGs configurations studied in this work, the theoretical P_{max} values are 177.5 and 326.6 µW/cm² respectively for the 2- and 3-membranes modules, if the Seebeck coefficient and electrical conductivities of the Chromel and Constantan are optimum (ie. $\alpha_{TC} = 63$ µV/K and R_{int} resp. equals to 190.6 or 79.9 Ω).

Finally, one can underline that P_{max} depends on the geometrical dimensions of the thermoelements (length, width and thickness) and their number, because these are *all involved in both the thermal and electrical aspects* of the µTEG. So, *a priori*, with this modeling, we can vary all the geometric dimensions and look for one or several optimum output power as a function of several parameters, as membrane number. This will be presented in a future work, as *for this first study we directly focused on technological fabrication of the new module*.

4. Fabrication and characterization

4.1 Fabrication of µTEGs

The 2.5D µTEG realization is based on the silicon technology starting with 3-inch, 380 µm thick, double-sided polished (100) Silicon wafers, to fabricate the two parts of the device, the folded thermopile on suspended membranes and the top concentrator. Several modules can be fabricated on each wafer. The flow chart of the microfabrication processes is given in Fig. 8 for the implementation of a thermopile suspended onto 2 membranes. For simplicity of the drawing, 32 TCs are displayed. In reality, for the 2- or 3-membranes µTEGs, the thermopile cumulates respectively 100 TCs (on 4 branches) or 150 TCs (on 6 branches), for identical footprint $A_{\mu TEG}$ and identical number of TCs per parallel branch (N_S = 25 TCs).

The process is started by the deposition of SiO_2/Si_xN_y (800/600 nm) bilayer on both sides of the substrate (Fig. 8(b)) by LPCVD (Low Pressure Chemical Vapor Deposition) using a TEMPRESS® furnace. The thicknesses of the SiO_2 and Si_xN_y layers are adjusted to compensate their respective stresses and allow the mechanical stability of the membranes (tensile stress less than 100 MPa [44]). Moreover, this bilayer is also used as a physical mask on the backside during the etching of the Silicon substrate to liberate the membrane areas.

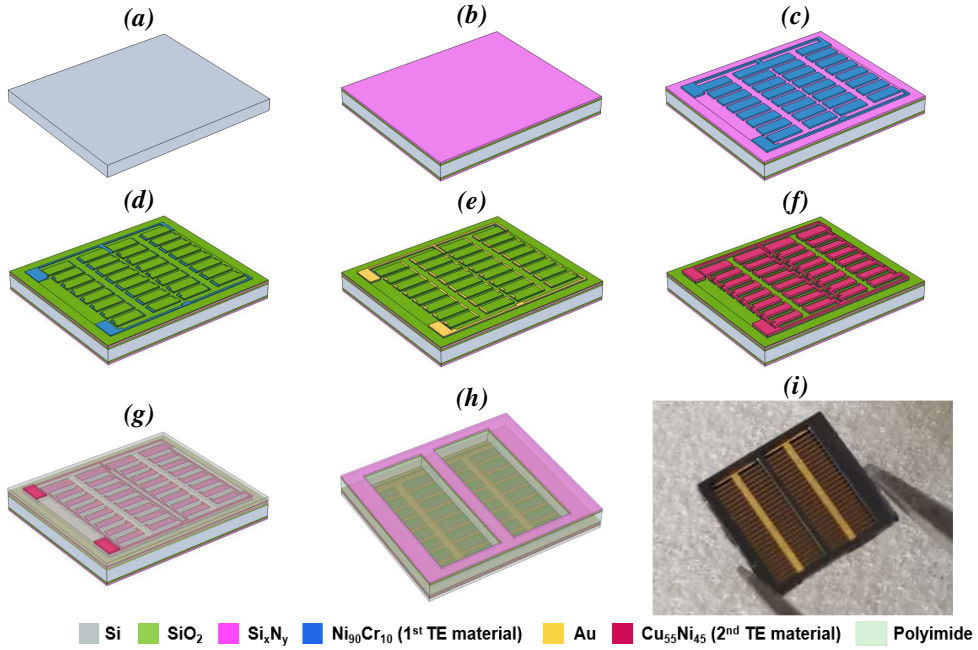

***Fig. 8** : Flow chart of the suspended membrane fabrication process. (a) Double-sided polished Si substrate; (b) LPCVD growth of SiO_2/Si_xN_y on both sides of the substrate; (c) Sputtering deposition and patterning of $Ni_{90}Cr_{10}$; (d) PECVD of SiO_2 and patterning; (e) Metallization of the contacts with Ti/Au layer; (f) Sputtering deposition and patterning of $Cu_{55}Ni_{45}$ via lift-off; (g) Passivation deposition of a thick Polyimide layer; (h) Backside DRIE etching for opening the cavities and release the membranes; (i) Optical photograph of the suspended membranes seen from the backside after the Silicon deep etching.*

Then a 150 nm thick $Ni_{90}Cr_{10}$ layer is deposited onto the SiO_2/Si_xN_y bilayer by Radio-Frequency magnetron sputtering at room temperature, using an Alliance Concept DP 650 machine. A much thicker layer could have been

better but this will require further complementary technological developments to solve a delamination problem that ultimately occurs during thermopile fabrication. A mixture of hydrochloric acid and nitric acid, known as "aqua regia", was used to etch the $Ni_{90}Cr_{10}$ in order to make the TE strips (Fig. 8(c)). The chemical etching has been optimized to control the etching rate and reduce the under-etching phenomena. A thin SiO_2 layer (150nm) was then deposited by PECVD (Plasma Enhanced Chemical Vapor Deposition) using an Oxford Plasmalab 80 Plus system at 300°C. The RIE (Reactive Ionic Etching) process employing a CF_4/CHF_3 gas mixture was used to etch the SiO_2 layer in order to get access to the thermopile contact pads, and to the areas of the $Ni_{90}Cr_{10}$ strips that will be in contact with the second thermoelement as illustrated in Fig. 8(d). A layer of metals Ti:10 nm/Au:100 nm, is deposited by evaporation and lift-off process, used at the contacts level (Fig. 8(e)) to ensure a good electrical contact between the junctions of the thermoelements.

The $Cu_{55}Ni_{45}$ strips (450 nm thick), representing the second thermoelement, are then periodically deposited by sputtering and lift-off on $Ni_{90}Cr_{10}$ strips as shown in Fig. 8(f). Here the thickness of Constantan was less an issue for the technology, opposite to the first thermoelement case (Chromel). A 12 µm thick layer of photosensitive Polyimide HD4110 is deposited by spin-coating all over the thermopile and then is opened on the contact pads by photolithography means (Fig. 8(g)). Finally, a backside DRIE (Deep Reactive Ionic Etching) of the Si substrate, based on Bosch process [49], was implemented to dig completely the substrate until the multilayer encapsulating the thermopile (Fig. 8(h)) on the front-side of the wafer: the suspended membranes are realized and well visible (Fig. 8(i)).

The second part of the module (concentrator) is made from another Si wafer (Fig. 9(a)). First, a 2µm thick SiO_2 passivation layer is grown by LPCVD on both sides of the wafer (Fig. 9(b)). This layer is used as a physical mask on the backside during the etching of the Si substrate to build up the concentrator pillars and the mechanical holding bosses. A meander-shaped metallic heater (Ti:20 nm/Au:250 nm) is first deposited by evaporation and lift-off process on the front-side of the wafer (Fig. 9(c)). Finally, the pillars and bosses were made in backside of the wafer by DRIE of Si as shown in Fig. 9(d), (e) and (f): the etching is 230 µm deep and corresponds to the aimed height of the pillars. The resistance of the heater varies between 10 and 14.5 Ω.

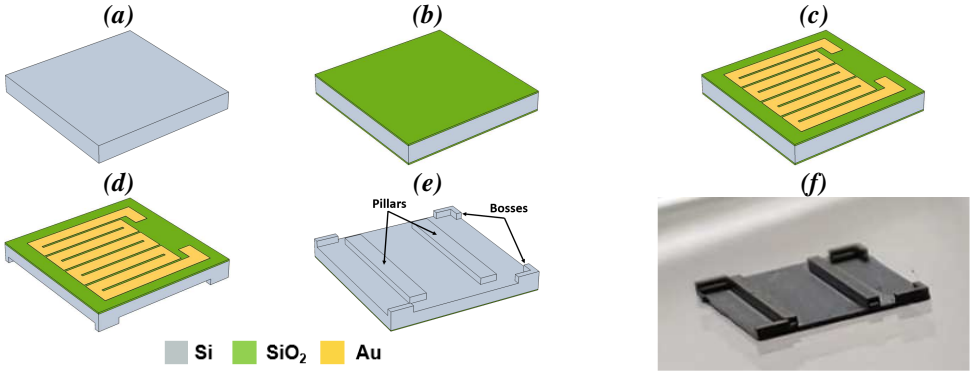

***Fig. 9** : Flow chart of the main steps of the heat concentrator fabrication process. (a) Double-sided polished Silicon wafer; (b) LPCVD SiO_2 growth on both sides of the wafer; (c) Realization of the metallic (Ti/Au) heater on the wafer front-side; (d) and (e) Fabrication of the pillars and bosses on the backside of the wafer by DRIE etching; (f) Image of the backside of a 2-pillars concentrator that will serve for the 2-membranes µTEG.*

Fig. 10 illustrates the 2.5D µTEG module after the assembly of the concentrator on the folded thermopile. Considering the surface chosen for each module (~1/3 cm²) it is possible to accommodate 44 modules per 3-inch Si wafer, to which are added some test patterns for the electrical and Seebeck measurements of the TE layers.

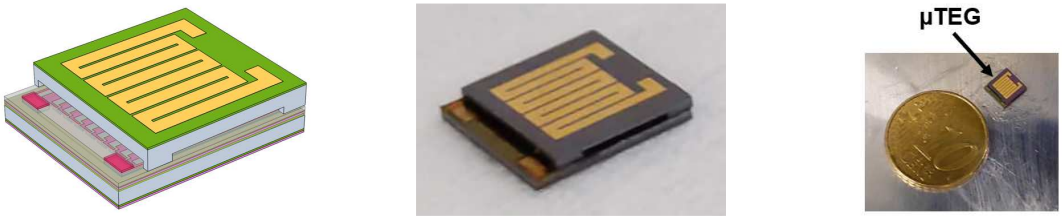

***Fig. 10** : Final images of the µTEG after assembly of the concentrator and the suspended membranes.*

The transfer of the concentrator onto the suspended membranes has, in the past, exploited the implementation of a sealing technique by thermocompression [42]. However, this technique is expensive and technologically complicated, and can lead to mechanical rupture of the membranes. For practical reasons, the alignments between the concentrator and the suspended membranes are performed, in this work, under optical microscopy using alignment wedges. In addition, some thermal grease is used to ensure a good wet contact between concentrator pillars and membranes (and substrate on heat sink) in order to minimize thermal contact resistances.

4.2 Properties of thermoelectric materials

As mentioned in the previous section, we have integrated, in our manufacturing masks, test patterns adapted to our characterization setups (electrical resistivity and Seebeck coefficient). These test patterns are thus issued from the same wafer and the same layers of Chromel and Constantan as those used in the µTEGs.
The Seebeck coefficients of $Ni_{90}Cr_{10}$ and $Cu_{55}Ni_{45}$ are measured as a function of temperature (range 20 -100°C) using a homemade set-up and a measurement protocol described in detail in [50]. Fig. 11 shows the variation of Seebeck coefficient of $Ni_{90}Cr_{10}$ and $Cu_{55}Ni_{45}$ as a function of the average temperature (the lowest value of average temperature, 35°C, was imposed by the experimental real ambient temperature).
For each material, several measurements have been performed on several patterns located in different areas, in order to deduce the range of variation of the Seebeck coefficient over the 3-inch wafer.

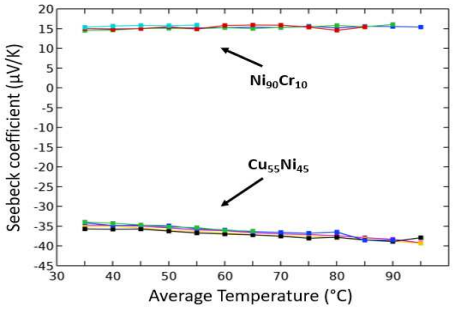

***Fig. 11** : Seebeck coefficient of $Ni_{90}Cr_{10}$ and $Cu_{55}Ni_{45}$ versus average temperature.*

In the working temperature range, we measured an almost constant value of the Seebeck coefficient for the 150nm thick $Ni_{90}Cr_{10}$ layer (with an average deviation lower than 1µV/K). On the other hand, the Seebeck coefficient of the 450nm thick $Cu_{55}Ni_{45}$ layer increases slightly (in absolute value) as a function of the average temperature with a deviation lower than 3 µV/K.

So, the average values of the Seebeck coefficients at room temperature, extrapolated from measurements in Fig. 11, are about +15 µV/K for $Ni_{90}Cr_{10}$ and –33 µV/K for $Cu_{55}Ni_{45}$ (Table 2). This results in an *equivalent Seebeck coefficient of a thermocouple* of about α_{TC} = 48 µV/K. In a separate optimization work, carried out on calibration wafers that cannot yet be transferred into the 2.5D µTEG microfabrication process, because of delamination and cracking issues (not shown here), we found higher values of the thermopower and electrical conductivity for both thermoelements, when using a higher deposition temperature (for Constantan) or using an annealing stage at high temperature (for Chromel). The TC Seebeck coefficient would have been 64 µV/K if both optimized layers could be used in the folded TCs.

The characterization of the electrical resistivity of $Ni_{90}Cr_{10}$ and $Cu_{55}Ni_{45}$ is carried out using a four-probe Accent® probing station HL5500 PC. This allows semi-automatic measurements of the electrical resistivity using the Van Der Pauw configuration (clover-leaf-shaped samples). The electrical resistivities of $Ni_{90}Cr_{10}$ and $Cu_{55}Ni_{45}$ measured at room temperature and the calculated values of power factor, α^2/ρ, are summarized in Table 2. These obtained TE properties show that the *quality of the deposited layers is moderate* compared to the published values of the state of the art [51–56] and compared to our own optimum layers as stated earlier. Obviously, in future work we will have to implement an adaptation of our technological process of "folded thermopile" to be compatible with the required high temperature extra steps needed to have high quality Constantan and Chromel.

TE material	Thickness (nm)	Seebeck coefficient α (µV/K)	Electrical resistivity ρ (µΩ.cm)	Power Factor α^2/ρ ($\mu W.cm^{-1}.K^{-2}$)
$Ni_{90}Cr_{10}$	150	15	100.3	2.24
$Cu_{55}Ni_{45}$	450	– 33	59.8	18.21

***Table 2** : Thermoelectric properties of $Ni_{90}Cr_{10}$ and $Cu_{55}Ni_{45}$ at 298K.*

4.3 Performance of the µTEGs

In this work, each fabricated 2.5D µTEG based on Constantan/Chromel thermopile was characterized using the four-probe set-up shown in Fig. 12. The measurement principle consists in injecting a thermal power by Joule effect in the heater with two probes, and measuring with two other probes the Seebeck voltage generated by the thermopile. The module under characterization is mounted on a large Aluminum block used as a heat sink to evacuate heat and keep the backside of the µTEG at room temperature. The thermal power dissipated in the concentrator is deduced from the direct measurements of the current flowing through the heater and the voltage at its terminals. The injected current is adjusted between 0 and 290 mA, which corresponds to a thermal power dissipated ranging from 0 to 1.2 W. At the output of the µTEG, the Seebeck voltage generated is measured (using a high impedance voltmeter) as a function of the thermal power injected into the concentrator.

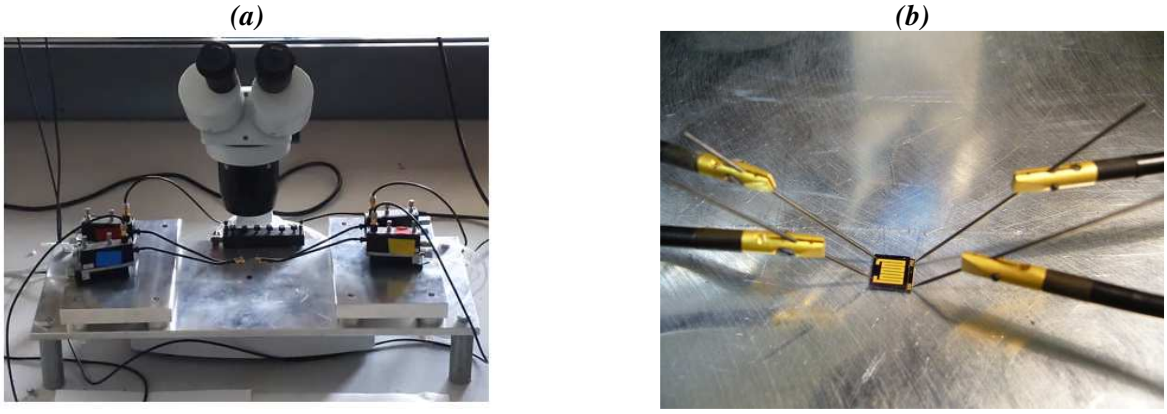

***Fig. 12** : (a) Photos of the four-probe set-up used for the µTEG characterization; (b) Zoom on a µTEG positioned under 4 probes (2 are used to inject the current in the heater and the 2 others for the Seebeck voltage measurement).*

The characteristics of both µTEG configurations realized and characterized in this work are presented in the Table 3. As stated earlier, the 2- or 3-membranes based modules have respectively 100 or 150 TCs with a series/parallel assembly. The thermoelement length and the strip width are also given in the table.

Module configuration	Number of membranes	TC length (µm)	Strip width (µm)		Number of TCs	Internal electrical resistance (Ω)
			$Ni_{90}Cr_{10}$	$Cu_{55}Ni_{45}$		
2m-µTEG	2	1060	200	150	100	305
3m-µTEG	3	670	200	150	150	140

***Table 3** : Main parameters of the 2 fabricated and characterized µTEG configurations.*

We note that as expected, the internal electrical resistance of these new metal-based µTEGs, is clearly lower than the one of our first generation of µTEGs, based on a polySilicon/metal thermopiles: in this former case, resistances were of the order of a hundred kΩ to a few MΩ for modules with 2 membranes [33, 43], while for the new family it is one to three hundred Ω. This drastic reduction of resistances results from the use of TE metals ($Ni_{90}Cr_{10}$ and $Cu_{55}Ni_{45}$) with very low electrical resistivity, as well as from the new topology of the thermopile in which one part of the TCs are associated in parallel.

Fig. 13 shows the measured output Seebeck voltage (V_{out}) that was generated, as a function of the Joule input power (ϕ_i) injected into the concentrator. Each module is characterized several times to reduce the error related to any possible misalignment of the concentrator. Only the best reproducible results are presented in this figure. To avoid overheating of the modules, we have limited the maximum input power to harvest to about 1.2 W. For each characterization, the temperature of the heat sink is measured with a probe placed close to the µTEG: it shows a quasi-no heating over the duration of the measurement thanks to the efficient heat sink dissipator. We assumed that for each characterization, ϕ_i was fully injected into the concentrator and was dissipated to the heat sink through the µTEG (neglected the part exchanged with the ambient air).

The experimental $V_{out}(\phi_i)$ characteristics are almost linear and this linear characteristic of the output voltage as a function of ϕ_i are consistent with the Seebeck effect. Indeed, i/ on one hand, $V_{out} = N_s \alpha_{TC} \Delta T_{hc}$, where N_s=25 for a stripe width of 200µm, $\alpha_{TC} = (\alpha_{NiCr} - \alpha_{CuNi}) = 48$ µV/K, and ii/ on the other hand, if R_i^{th} is the *internal thermal resistance* of the µTEG, then the effective temperature difference between the hot and cold junctions of each thermocouple is given by $\Delta T_{hc} = R_i^{th} \phi_i$. At the end: $V_{out} = N_s \alpha_{TC} R_i^{th} \phi_i$, so finding linearity is obvious (R_i^{th} is independent of the flux).

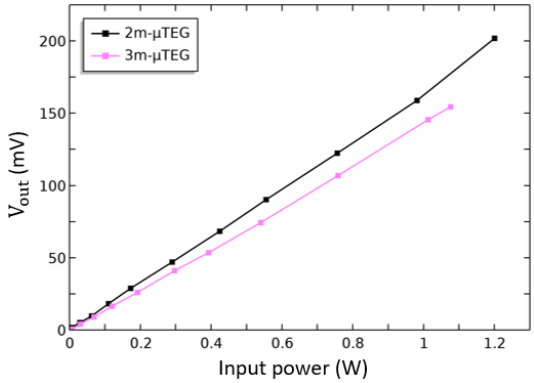

***Fig. 13** : Seebeck voltage generated in 2- and 3-membranes µTEGs versus input power injected into the concentrator.*

Incidentally, one can deduce the internal thermal resistance from this relation: R_i^{th} is 137 K/W and 120 K/W respectively for the 2- and 3-membranes µTEGs. So the thermal resistance of the novel µTEG is pretty high, nevertheless it depends on the number of membranes (ie. fixed by the TCs length) so R_i^{th} is likely to decrease if we fabricate modules with even more membranes (ie. much shorter TCs).
The highest V_{out} delivered (about 201.6 mV) is obtained for the µTEG with 2 membranes for a maximum injected thermal power of 1.2 W while it is some 11% lower for the 3-membranes µTEG (consistent with a lower ΔT_{hc} for the same ϕ_i, due to shorter TCs).

The maximum output power generated by the µTEG, P_{max}, can be calculated as stated earlier, using the measured Seebeck voltage V_{out} and the experimental internal electrical resistance R_{int} (305 Ω and 140 Ω respectively for 2- and 3-membranes µTEGs, Table 3): $P_{max} = V_{out}^2/4R_{int}$. The evolution of P_{max} generated as a function of ϕ_i injected into the concentrator is presented in Fig. 14 for the two µTEG configurations.

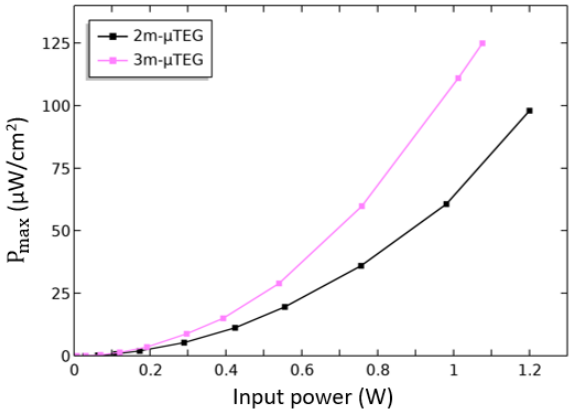

***Fig. 14** : Maximum output power density generated versus input power injected into the concentrator.*

These results show that the 3-membranes µTEG configuration has the best performance as was expected from our modelling. Its highest experimental value is about 125 µW/cm² for ϕ_i ~1.07 W. Normalized to 1W of injected heat, this corresponds to an output power of 108.3 µW/cm². For the 2-membranes based µTEG, P_{max} is as expected smaller: it is about 64 µW/cm². This is still higher than the best P_{max} obtained for the 2-membranes polySi-based µTEGs, with a standard thermopile (50 - 62 µW/cm² [43]) which is encouraging.
However, *these both experimental performances are lower than the predicted values* (see section 3.3, it is 50% lower for the 3-membranes µTEG) in part because the experimental Seebeck and electrical properties of the Chromel and Constantan layers used in the fabricated modules, are not the optimized ones. Anyway, as the thermogeneration gets better with the increase of membrane number (ie with the shortening of TCs), *we expect, as for our former µTEG geometry (polySi based)*, to obtain an optimum value of P_{max} for an even higher number of membranes. This will be explored in a forthcoming work.

The above-mentioned best experimental µTEG performance has been compared to the ones of the state-of-the-art modules also based on metallic thermoelectrics: these are listed in Table 4. In this table we reported a factor used in the literature for comparing the performance of µTEGs, regardless of their topology or configuration: it is defined by the ratio $F_e = P_{max}/(A_{\mu TEG}\,\Delta T_{ext}^2)$, where $A_{\mu TEG}$ is the area of the µTEG and ΔT_{ext} is the temperature difference between the external surfaces of µTEG (ΔT_{HC} in our work). This factor F_e is often called "efficiency factor" (see for instance [33,57]). The use of this factor was first proposed by Strasser *et al.* [58] almost two decades ago.

TE material	Area of µTEG (mm²)	Number of TCs	R_{int} (Ω)	ΔT_{ext} (K)	V_{out} (V)	P_{max} (µW/cm²)	F_e (µW.cm^{-2}.K^{-2})	Ref
NiCr/CuNi	34	150	140	126	0.143	108.3	6.82×10^{-3}	This work
NiCr/CuNi	900	33	--	22.7	0.3	0.41	8×10^{-4}	[59]
NiCr/CuNi	768	40	392	250	0.53	19.53	3.12×10^{-4}	[60]
Cu/CuNi	250	50	56000	70	2.18	8.5	1.73×10^{-3}	[61]
Cu/Ni	1118	10	7.41	69	0.013	0.51	1.07×10^{-4}	[62]
Ag/Ni	383	216	--	127	--	80.4	4.98×10^{-3}	[63]

***Table 4** : Comparison of the performance obtained in this work with the state-of-the-art metallic based µTEGs.*

In this comparison, our 3-membranes µTEG is the one that integrates the largest number of TCs despite its very small area, compared to other µTEGs. This is one of the main advantages of the proposed folded thermopile topology, that presents a high integration density of TCs. This results into better values for P_{max} and for the efficiency factor: F_e is about 6.82×10^{-3} µW.cm^{-2}.K^{-2} (ΔT_{ext}=ΔT_{HC}= 126 K, deduced from the experimental ΔT_{hc}=

120 K and using our simulation presented in section 3.3). This factor is pretty good when compared to the other literature values (modules with metal TCs) and even compared to our own former µTEG topology (polySi-based standard thermopile), where F_e was ranging from 1.3×10^{-3} to 9×10^{-3} µW.cm^{-2}.K^{-2} in 2-membrane based modules.

Of course, one can find in literature larger values if considering µTEGs that integrate other kind of TE compounds (not metals) in bulk, thin or thick layer form, as shown in Selvan *et al.* [57] who proposed a methodological survey on efficiency factors published from 1989 to 2017. If one assumes this study is still valid today, our 3-membrane metal-based µTEG would be in the average. Indeed owing to this survey: "*44.1% of thick and thin film thermoelectric generators are realizing in between 0.001 and 4 µW.cm^{-2}.K^{-2}, while 43.1% of thick and thin films are earning among 10^{-6} to 0.001 µW.cm^{-2}.K^{-2}*" [57]. In addition, another comprehensive review has been proposed very recently by Yang et al [64], however it is focused on polySi-based miniature modules.

Anyway, those first performance results of our new 2.5D µTEG validate the interest of our folded series/parallel planar architecture. It also deserves to be improved further by i/ on one hand, optimizing the quality of the two TEs (Chromel and Constantan) as stated before, and ii/ on the other hand, by looking for the optimum dimension in terms of membrane number (ie TC length and number). We already know from our studies on our former µTEG geometry (polySi/metal series thermopile) that the best efficiency factor we could experimentally obtain (F_e=0.117 µW.cm^{-2}.K^{-2} [43]) was when using shorter TCs, in a 10-membranes based module. All these points constitute the next steps in our technological roadmap.

5. Conclusions

We report on a novel 2.5D µTEG integrating a planar thermopile with periodically folded $Ni_{90}Cr_{10}$ /$Cu_{55}Ni_{45}$ thermocouples and distributed on 2- or 3-membranes. Our new topology has an increased TC integration density and a reduced module internal electrical resistance, due to the electrical association in "series and parallel" of the TCs and the use of metallic thermoelectrics. The two µTEG configurations, with 2 and 3 membranes, have been successfully modeled, manufactured, and characterized. The best maximum output power density is about 108.3 µW/cm^2 for 1W heat injected on the concentrator and as predicted is delivered by the 3-membranes µTEG. This corresponds to a 126 K temperature difference between the external surfaces of the module and so to an efficiency factor of 6.82×10^{-3} µW.cm^{-2}.K^{-2}. This performance is better than in the state-of-the-art modules using metallic thermoelectrics. Also, the new modules thermal resistance are pretty high: 120 to 137 K/W. In upcoming work the focus will be on improving the performances of the novel µTEG by i/ optimizing the geometrical parameters as the membrane number and ii/ by solving technical issues as thermal budget in order to be able to employ $Ni_{90}Cr_{10}$ and $Cu_{55}Ni_{45}$ layers with optimum thicknesses and TE properties.

Declaration of Competing Interest

The authors declare that they have no known competing financial interests or personal relationships that could have appeared to influence the work reported in this paper.

Acknowledgements

This research work has been partly undertaken with the support of IEMN fabrication facility (CMNF), which is a member of the French Technology Network RENATECH.

References

[1] "IoT connected devices worldwide 2019-2030", *Statista*. https://www.statista.com/statistics/1183457/iot-connected-devices-worldwide/.
[2] "Lithium-ion batteries need to be greener and more ethical," *Nature*, vol. 595, no. 7865, pp. 7–7, Jun. 2021. doi: 10.1038/d41586-021-01735-z.
[3] W. Mrozik, M. Ali Rajaeifar, O. Heidrich, and P. Christensen, *Energy Environ. Sci.*, vol. 14, pp. 6099–6121, 2021. doi: 10.1039/D1EE00691F.
[4] L. Vandepaer, J. Cloutier, and B. Amor, *Renew. Sustain. Energy Rev.*, vol. 78, pp. 46–60, Oct. 2017. doi: 10.1016/j.rser.2017.04.057.
[5] D. M. Rowe, Ed., *Thermoelectrics handbook: macro to nano*. Boca Raton: CRC/Taylor & Francis, 2006.
[6] G. J. Snyder and E. S. Toberer, *Nat. Mater.*, vol. 7, pp. 105–114, Feb. 2008. doi: 10.1038/nmat2090.
[7] T. J. Seebeck, *Abh K Akad Wiss Berl.*, pp. 290–346, 1821.
[8] A. Kumar, S. Bano, B. Govind, A. Bhardwaj, K. Bhatt, D. K. Misra, *J. Electron. Mater.*, vol. 50, pp. 6037–6059, Nov. 2021. doi: 10.1007/s11664-021-09153-7.
[9] Z.-G. Chen, G. Han, L. Yang, L. Cheng, and J. Zou, *Prog. Nat. Sci. Mater. Int.*, vol. 22, pp. 535–549, Dec. 2012. doi: 10.1016/j.pnsc.2012.11.011.
[10] G. A. Slack and V. G. Tsoukala, *J. Appl. Phys.*, vol. 76, pp. 1665–1671, Aug. 1994. doi: 10.1063/1.357750.
[11] L. D. Hicks and M. S. Dresselhaus, *MRS Proc.*, vol. 326, p. 413, Jan. 1993. doi: 10.1557/PROC-326-413.
[12] L. D. Hicks and M. S. Dresselhaus, *Phys. Rev. B*, vol. 47, pp. 16631–16634, Jun. 1993. doi: 10.1103/PhysRevB.47.16631.
[13] L. D. Hicks and M. S. Dresselhaus, *Phys. Rev. B*, vol. 47, pp. 12727–12731, May 1993. doi: 10.1103/PhysRevB.47.12727.
[14] O. Caballero-Calero, J. R. Ares, and M. Martín-González, *Adv. Sustain. Syst.*, p. 2100095, Jun. 2021. doi: 10.1002/adsu.202100095.
[15] K. V. Selvan and M. S. Mohamed Ali, *Renew. Sustain. Energy Rev.*, vol. 54, pp. 1035–1047, Feb. 2016. doi: 10.1016/j.rser.2015.10.046.

[16] A. Nozariasbmarz *et al.*, *Appl. Energy*, vol. 258, p. 114069, Jan. 2020. doi: 10.1016/j.apenergy.2019.114069.
[17] S. Shittu, G. Li, X. Zhao, and X. Ma, *Appl. Energy*, vol. 268, p. 115075, Jun. 2020. doi: 10.1016/j.apenergy.2020.115075.
[18] N. Jaziri, A. Boughamoura, J. Müller, B. Mezghani, F. Tounsi, and M. Ismail, *Energy Rep.*, vol. 6, pp. 264–287, Dec. 2020. doi: 10.1016/j.egyr.2019.12.011.
[19] F. Tohidi, S. Ghazanfari Holagh, and A. Chitsaz, *Appl. Therm. Eng.*, vol. 201, p. 117793, Jan. 2022. doi: 10.1016/j.applthermaleng.2021.117793.
[20] M. Kishi *et al.*, in *18th Int. Conf. on Thermoelectrics. Proceedings ICT'99,* Baltimore, MD, USA, 1999, pp. 301–307. doi: 10.1109/ICT.1999.843389.
[21] Y. Li, K. Buddharaju, B. C. Tinh, N. Singh, and S. J. Lee, *IEEE Electron Device Lett.*, vol. 33, pp. 715–717, May 2012. doi: 10.1109/LED.2012.2187424.
[22] H. Bottner, J. Nurnus, A. Schubert, and F. Volkert, in *26th Int. Conf. on Thermoelectrics*, Jeju Island, South Korea, Jun. 2007, pp. 306–309. doi: 10.1109/ICT.2007.4569484.
[23] R. Venkatasubramanian, C. B. Watkins, C. Caylor, and G. Bulman, presented at the The 6th Int. Workshop on Micro and Nanotechnology for Power Generation and Energy Conversion Applications, Berkeley, U.S.A, Dec. 2006.
[24] G. J. Snyder, J. R. Lim, C.-K. Huang, and J.-P. Fleurial, *Nat. Mater.*, vol. 2, pp. 528–531, Aug. 2003. doi: 10.1038/nmat943.
[25] G. Hu, H. Edwards, and M. Lee, *Nat. Electron.*, vol. 2, pp. 300–306, Jul. 2019. doi: 10.1038/s41928-019-0271-9.
[26] R. Roth, R. Rostek, K. Cobry, C. Kohler, M. Groh, P. Woias, *J. Microelectromechanical Syst.*, vol. 23, pp. 961–971, Aug. 2014. doi: 10.1109/JMEMS.2014.2303198.
[27] S. Liu, B. Hu, D. Liu, F. Li, JF. Li, B. Li, L. Li, YH. Lin and CW. Nan, *Appl. Energy*, vol. 225, pp. 600–610, Sep. 2018. doi: 10.1063/1.5074184.
[28] S. Elyamny, E. Dimaggio, S. Magagna, D. Narducci, and G. Pennelli, *Nano Lett.*, vol. 20, pp. 4748–4753, Jul. 2020. doi: 10.1021/acs.nanolett.0c00227.
[29] J. Yan, X. Liao, D. Yan, and Y. Chen, *J. Microelectromechanical Syst.*, vol. 27, pp. 1–18, Feb. 2018. doi: 10.1109/JMEMS.2017.2782748.
[30] D. M. Rowe, D. V. Morgan, and J. H. Kiely, *Electron. Lett.*, vol. 25, p. 166, 1989. doi: 10.1049/el:19890120.
[31] M. Strasser, R. Aigner, M. Franosch, and G. Wachutka, *Sens. Actuator A-Phys.*, vol. 97–98, pp. 535–542, Apr. 2002. doi: 10.1016/S0924-4247(01)00815-9.
[32] Z. Wang, Y. van Andel, M. Jambunathan, V. Leonov, R. Elfrink, and R. J. M. Vullers, *J. Electron. Mater.*, vol. 40, pp. 499–503, May 2011. doi: 10.1007/s11664-010-1402-2.
[33] Z. Yuan, K. Ziouche, Z. Bougrioua, P. Lejeune, T. Lasri, and D. Leclercq, *Sens. Actuator A-Phys.* vol. 221, pp. 67–76, Jan. 2015. doi: 10.1016/j.sna.2014.10.026.
[34] D. Tainoff, A. Proudhom, C. Tur, T. Crozes, S. Dufresnes, S. Dumont, D. Bourgault, O. Bourgeois, *Nano Energy*, vol. 57, pp. 804–810, Mar. 2019. doi: 10.1016/j.nanoen.2019.01.006.
[35] ID. Noyan, G. Gadea, M. Salleras, M. Pacios, C. Calaza, A. Stranz, M. Dolcet, A. Morata, A. Tarancon, L. Fonseca *Nano Energy*, vol. 57, pp. 492–499, Mar. 2019. doi: 10.1016/j.nanoen.2018.12.050.
[36] S. El Oualid, F. Kosior, A. Dauscher, C. Candolfi, G. Span, E. Mehmedovic, J. Paris, B. Lenoir, *Energy Environ. Sci.*, vol. 13, pp. 3579–3591, 2020. doi: 10.1039/D0EE02579H.
[37] Y. Yu, W. Zhu, Y. Wang, P. Zhu, K. Peng, and Y. Deng, *Appl. Energy*, vol. 275, p. 115404, Oct. 2020. doi: 10.1016/j.apenergy.2020.115404.
[38] G. Savelli, JP. Colonna, P. Coudrain, P. Faucherand, A. Royer, LM. Collin, A. Amnache, L. Fréchette, *Energy*, vol. 252, p. 123984, Aug. 2022. doi: 10.1016/j.energy.2022.123984.
[39] S. M. Yang and Y. J. Huang, *Sens. Actuator A-Phys*, vol. 344, p. 113689, Sep. 2022. doi: 10.1016/j.sna.2022.113689.
[40] R. He, G. Schierning, and K. Nielsch, *Adv. Mater. Technol.*, vol. 3, p. 1700256, 2018. doi: 10.1002/admt.201700256.
[41] S. M. Yang, T. Lee and M. Cong, *Sens. Actuator A-Phys.* vol. 157, pp.258-266, 2010. doi: 10.1016/j.sna.2009.11.023.
[42] K. Ziouche, Z. Yuan, P. Lejeune, T. Lasri, D. Leclercq, and Z. Bougrioua, *J. Microelectromechanical Syst.*, vol. 26, pp. 45–47, Feb. 2017. doi: 10.1109/JMEMS.2016.2633442.
[43] Z. Bougrioua, I. Bel−Hadj, K. Ziouche, in *17th Europ. Conf. on Thermoelectrics*, Limassol, Cyprus, Sept. 2019. https://hal.archives-ouvertes.fr/hal-02906736
[44] M. Haffar, These de doctorat, Lille 1, 2007. Available: https://www.theses.fr/2007LIL10053.
[45] COMSOL, 2016a. Heat Transfer Module User's Guide. COMSOL Multiphysics® v.5.2a. https://www.comsol.fr.
[46] K. E. Goodson, M. I. Flik, L. T. Su, and D. A. Antoniadis, *IEEE Electron Device Lett.*, vol. 14, pp. 490–492, Oct. 1993. doi: 10.1109/55.244740.
[47] X. Zhang and C. P. Grigoropoulos, *Rev. Sci. Instrum.*, vol. 66, pp. 1115–1120, Feb. 1995. doi: 10.1063/1.1145989.
[48] B. Sundqvist, *J. Appl. Phys.*, vol. 72, pp. 539–545, Jul. 1992. doi: 10.1063/1.351885.
[49] F. Laermer, A. Schilp, Method of anisotropically etching silicon, US5501893A, 1996.
[50] K. Ziouche, I. Bel-Hadj, and Z. Bougrioua, *Nano Energy*, vol. 80, p. 105553, Feb. 2021. doi: 10.1016/j.nanoen.2020.105553.
[51] R. V. Wilhelm and J. P. Roland, *J. Appl. Phys.*, vol. 48, pp. 2086–2088, May 1977. doi: 10.1063/1.323923.
[52] N. Sato and M. Takeda, in *ICT 2005. 24th Int. Conference on Thermoelectrics,* Clemson, SC, USA, 2005, pp. 175–178. doi: 10.1109/ICT.2005.1519912.
[53] P. K. Sharma, V. K. Sharma, T. D. Senguttuvan, and S. Chaudhary, *Measurement*, vol. 150, p. 107054, Jan. 2020. doi: 10.1016/j.measurement.2019.107054.
[54] A. Kumar, A. Patel, S. Singh, A. Kandasami, and D. Kanjilal, *Rev. Sci. Instrum.*, vol. 90, p. 104901, Oct. 2019. doi: 10.1063/1.5116186.
[55] F. Cougnon and D. Depla, *Coatings*, vol. 9, p. 299, May 2019. doi: 10.3390/coatings9050299.
[56] E. Castaño, E. Revuelto, M. C. Martín, A. García-Alonso, F. J. Gracia, *Sens. Actuator A-Phys.*, vol. 60, pp. 65–67, May 1997. doi: 10.1016/S0924-4247(96)01435-5.
[57] K. V. Selvan, M. N. Hasan, and M. S. Mohamed Ali, *Int. J. Energy Res.*, vol. 43, pp. 113–140, Jan. 2019. doi: 10.1002/er.4206.
[58] M. Strasser, R. Aigner, C. Lauterbach, T. F. Sturm, M. Franosch, and G. Wachutka, *Sens. Actuator A-Phys.*, vol. 114, pp. 362–370, Sep. 2004. doi: 10.1016/j.sna.2003.11.039.
[59] Y. Iwasaki and M. Takeda, in *2006 25th International Conference on Thermoelectrics*, Vienna, Aug. 2006, pp. 562–565. doi: 10.1109/ICT.2006.331376.
[60] Q. Chen, J. P. Longtin, S. Tankiewicz, S. Sampath, and R. J. Gambino, *J. Micromechanics Microengineering*, vol. 14, pp. 506–513, Apr. 2004. doi: 10.1088/0960-1317/14/4/010.
[61] Y. Shimizu, M. Mizoshiri, M. Mikami, J. Sakurai, and S. Hata, *J. Phys. Conf. Ser.*, vol. 1052, p. 012032, Jul. 2018. doi: 10.1088/1742-6596/1052/1/012032.
[62] K. V. Selvan and M. S. M. Ali, in *2018 IEEE Micro Electro Mechanical Systems (MEMS)*, Jan. 2018, pp. 665–668. doi: 10.1109/MEMSYS.2018.8346642.
[63] B. Iezzi, K. Ankireddy, J. Twiddy, M. D. Losego, and J. S. Jur, *Appl. Energy*, vol. 208, pp. 758–765, Dec. 2017. doi: 10.1016/j.apenergy.2017.09.073.
[64] S. M. Yang , L.A. Chung and H.R. Wang, Sens. Actuator A-Phys, vol. 346, p. 113890, Oct. 2022. doi: 10.1016/j.sna.2022.113890.

Authors Biography

Ibrahim Bel-Hadj received his Ph.D. in "Micro-nano-systems and Sensors" from Lille University in mid 2022, for his work at IEMN (Institute of Electronics, Microelectronics & Nanotechnology) on the fabrication and optimization of micro-thermoelectric generators. Since September 2022 he is a postdoctoral researcher at University of Strasbourg (Fr) where his research interests are focused on nanoparticle engineering and plasmonic biosensors.

Zahia Bougrioua is a senior researcher at CNRS whose expertise is in compound semiconductors and in thermoelectrics, from elaboration to characterization and device fabrication. She received her Ph.D. in Materials Sciences from Lille University in 1994. From 1995 to 2001, she worked on III-(As,P) compounds at Montreal Ecole Polytechnique (Ca), then on wide band-gap III-N at IMEC (Be). In 2001 she was appointed at CNRS, first at CRHEA (Fr) to develop III-N for transistor and light emission applications, then, at IEMN, where she mainly focus on micro-sensors and µthermogenerators.

Katir Ziouche is a full Professor at Lille University. He joined IEMN in 1996 and received his Ph.D. in Electronics in 1999. He is Lecturer at Lille Institute of Technology since 2000, where he teaches electrical engineering, electronics and thermodynamics. His main research interests at IEMN is the development of new processes for fabrication of thermal microdevices (µsensors and µthermogenerators), and he is involved in thermal and electrical characterisations of thermoelectrics. Since 2021, he started taking part to the technological development of nitrides power devices.

Graphical Abstract

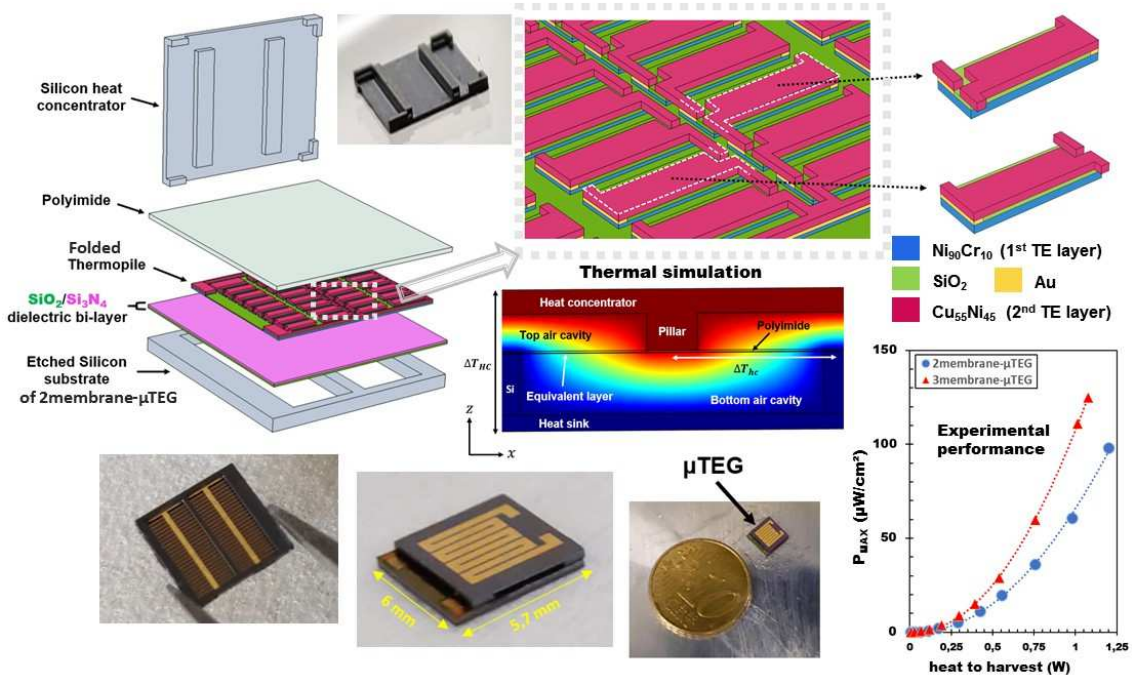

Highlights

- Multi-membrane-based 2.5D µTEGs integrating a new kind of metal-based thermopile are modeled, fabricated and characterized.
- The novel thermopile topology is periodically folded and is based on $Ni_{90}Cr_{10}$ and $Cu_{55}Ni_{45}$ thermoelectric layers.
- The thermopile integrates a high density of thermocouples with a combined series and parallel electrical association.
- In the 3-membranes based µTEG, a maximum output power density of 108.3 µW/cm^2 is generated from 1 W heat to harvest.
- Those 2.5D µTEGs have higher efficiency and thermal resistance than in the state of the art of metal based modules.